RSC Advances

PAPER

View Article Online
View Journal | View Issue

Cite this: *RSC Adv.*, 2025, **15**, 32894

A dual-fluorescence approach for turn-on ammonia and turn-off explosive picric acid detection *via* ESIPT inhibition: experimental, theoretical, and biological studies

Malavika S. Kumar and Avijit Kumar Das *

A fluorescent naphthalene–anthracene dyad (**AMN**) was developed as a dual-mode sensor for turn-on detection of ammonia (NH_3) and turn-off detection of picric acid (PA). **AMN** initially emits strong fluorescence at 427 nm due to excited-state intramolecular proton transfer (ESIPT), showing a large 62 nm Stokes shift. Upon PA addition, fluorescence is quenched and red-shifted to 463 nm. Conversely, NH_3 induces a red shift to 435 nm. These spectral responses are attributed to ESIPT inhibition *via* strong hydrogen bonding between the hydroxyl group of **AMN** and the analytes. **AMN** has been successfully applied in dipstick-based PA detection and as a low-cost food spoilage indicator for NH_3. Detection limits are 8.77 μM for PA and 5.29 μM for NH_3, with a Stern–Volmer constant of 5.62×10^5 M^{-1} for picric acid. Additionally, **AMN** shows ratiometric fluorescence upon interaction with BSA and ct DNA, accompanied by notable absorption changes. These findings, supported by UV-vis, fluorescence spectroscopy, NMR, molecular docking, and DFT studies, underscore the potential of **AMN** as a multifunctional fluorescent sensor for environmental and biological applications.

Received 15th July 2025
Accepted 4th September 2025

DOI: 10.1039/d5ra05068e

rsc.li/rsc-advances

1. Introduction

Recently, organized terror attacks all around the world have compelled scientists to develop effective techniques for detecting explosives. Nitro compounds constitute a significant percentage of common explosives. TNT was the most broadly used nitroaromatic compound (NAC) prior to World War I.[1–3] However, ascribed to its strong explosive force, picric acid (PA) has surfaced as an ideal substitute and has been employed as a raw material for lethal weapons.[4,5] It is extensively utilized in the pharmaceutical, dye, and rocket fuel industries.[6–9] The intake of PA can lead to anemia, cancer, cyanosis, liver problems, and skin and eye irritation.[10–14] Therefore, effectively monitoring and detecting trace amounts of PA in both vapor and solution phases is crucial for ensuring social and environmental safety.

On the other hand, several types of gas sensors have been designed and utilized for precarious gas sensing in various fields, including self-propelled manufacturing, ecological investigation, air quality control, therapeutic applications, and more. NH_3 (ammonia) is one of the most common caustic gases in the biosphere and is released through both industrial and natural activities.[15,16] In nature's nitrogen cycle, NH_3 is produced by the breakdown of organic nitrogen molecules in plants, human and animal waste, and the microbial decomposition of sewage.[17–19] Industrial processes such as metallurgical operations, mining, ceramic manufacturing, the synthesis of other chemical compounds, agricultural practices, and the use of domestic cleaning products also contribute to the artificial production of NH_3. Chronic exposure to NH_3 vapors can cause gastrointestinal illnesses, kidney problems, and nasal erosion ulcers.[20–22] Therefore, there is a critical need to develop effective sensor systems for the selective detection and monitoring of trace concentrations of NH_3 in the gas phase or NH_4^+ in the solution phase.

Recently, countless instrumentation techniques have become available for the detection and quantification of various analytes, including spectrophotometry, gas chromatography–mass spectrometry (GC–MS), flow spectroscopy, potentiometric electrodes, and infrared absorption. Electrochemical sensing is another widely used technology due to its high sensitivity and cost-effectiveness.[22–28] However, the aforementioned instrumentation techniques have limitations in practical usage for continuous analyte monitoring, as they often involve chemical usage, require extensive pre-treatment, depend on expensive apparatus, and are not advisable for on-site real-time monitoring.[29,30] To overcome these drawbacks, optical methods have emerged in recent years as efficient and practical solutions for sensing analytes under ambient conditions. Among these, fluorescence-based sensing techniques have gathered significant research interest due to their high detection sensitivity, low

Department of Chemistry, Christ University, Hosur Road, Bangalore, Karnataka, 560029, India. E-mail: avijitkumar.das@christuniversity.in

instrument cost, fast response time, and ease of use. Fluorescence-based sensing is particularly effective for detecting target analytes with high sensitivity.[31] In this respect, ESIPT (excited-state intramolecular proton transfer) phenomenon, a photo-induced proton transfer *via* an intramolecular hydrogen bond, is highly valued in organic optoelectronic materials for its photochemical and photophysical applications.[32] It occurs in molecules with intramolecular hydrogen bonding between donors and acceptors, involving rapid enol-to-keto phototautomerization ($>10^{12}$ s^{-1}), followed by radiative decay and reverse proton transfer (RPT) to restore the enol form (Scheme 2, pathway A). Its large Stokes shift enhances efficiency and minimizes self-absorption.[33] Common ESIPT fluorophores include derivatives of 2-(2′-hydroxyphenyl)benzimidazole, benzoxazole, benzothiazole, quinoline, benzophenones, flavones, anthraquinones, and benzotriazoles.[34] Herein, we have developed a ESIPT based Schiff base probe 2-((E)-1-(((Z)-anthracen-9-ylmethylene)hydrazineylidene)ethyl)naphthalen-1-ol **(AMN)**, for selective detection of picric acid and ammonia. The synthesis of **AMN** involved two steps involving reaction of 1-(1-hydroxynaphthalen-2-yl)ethan-1-one with hydrazine to produce compound 1 followed by its reaction with anthracene-9-carbaldehyde in ethanol to yield **AMN** (Scheme 1). The chemical structures of compound 1 and **AMN** were characterized using mass spectra and NMR analysis (Fig. S8–S10). Additionally, DNA and BSA binding studies were conducted to explore its potential biological applications. The interaction of Schiff-base ligands like **AMN** with DNA and BSA molecules has been investigated experimentally and theoretically in order to formulate new pharmacological medicines.[35,36] The amino acid residues can readily bind with drug molecules due to a large number of binding sites, which increases solubility and decreases toxicity.[37] Similarly, a drug molecule can attach to DNA by major or minor groove binding, hydrogen bonding/electrostatic interactions, or intercalation. Therefore, it is essential to comprehend how drugs interact with biomolecules in order to properly describe the pharmacokinetic profile and design of drugs.[38–41] For practical purposes, a low-cost food spoilage indicator was developed for NH_3 sensing, along with a dipstick method for the detection of picric acid.

2. Experimental

2.1 Materials and instrumentation

Sigma-Aldrich Chemicals Private Limited supplied the chemicals and solvents, which were used without any extra purification, unless stated otherwise. Melting points were found using an open-mouth capillary and a hot-plate melting point device. A Brucker 400 MHz device was employed to record ^{1}H-NMR spectra. DMSO-d_6 was utilized as the solvent and TMS as the internal standard for the NMR spectra. Chemical shifts are displayed in δ-units and the ^{1}H–^{1}H coupling constants are expressed in Hz. A PerkinElmer Lambda 30 UV-vis titration device was utilised for the UV-vis titration experiments, whereas a Shimadzu RF-5301 PC was utilised for the fluorescence experiment. A fluorescent cell with a 10-mm path was used in a fluorescence spectrofluorometer.

2.2 Synthesis and characterizations

2.2.1 Synthesis of compound 1. In a 100 mL round-bottom flask, 1-(1-hydroxynaphthalen-2-yl)-ethan-1-one (100 mg, 0.36 mmol) was dissolved in 10 mL of ethanol, followed by the dropwise addition of hydrazine. The reaction mixture was stirred at room temperature for 24 hours, resulting in the precipitation of compound 1. The precipitate was then filtered and washed sequentially with ethanol and ether to obtain a solid yellow product. (Yield: 80 mg, 75%).

^{1}H NMR (DMSO-d_6, 400 MHz): 14.91 (s, ^{1}H, –OH), 10.05 (s, ^{1}H), 8.21 (d, ^{1}H, $J = 7.6$ Hz), 7.79 (t, ^{1}H, $J = 8.8$ Hz), 7.58 (d, ^{1}H, $J = 8.8$ Hz), 7.46 (m, 2H), 7.32 (d, 2H, $J = 8.8$ Hz), 6.61 (s, 2H), 2.25 (s, 3H).

2.2.2 Synthesis of AMN. Compound 1 (100 mg, 0.5 mmol) was reacted with anthracene-9-carbaldehyde (103 mg, 0.5 mmol) in 12 mL of ethanol in a 100 mL round-bottom flask for 48 hours at room temperature. The reaction progress was monitored by TLC, and an orange solid precipitate was formed. Upon completion of the reaction, the precipitate was filtered, washed with ethanol and diethyl ether followed by vacuum-dried to obtain an orange solid.

(Yield: 150 mg, 77%). Mp: 200–210 °C. ^{1}H NMR (DMSO-d_6, 400 MHz): 15.35 (s, ^{1}H, –OH), 10.05 (s, ^{1}H), 8.89 (t, 2H, $J = 15.6$

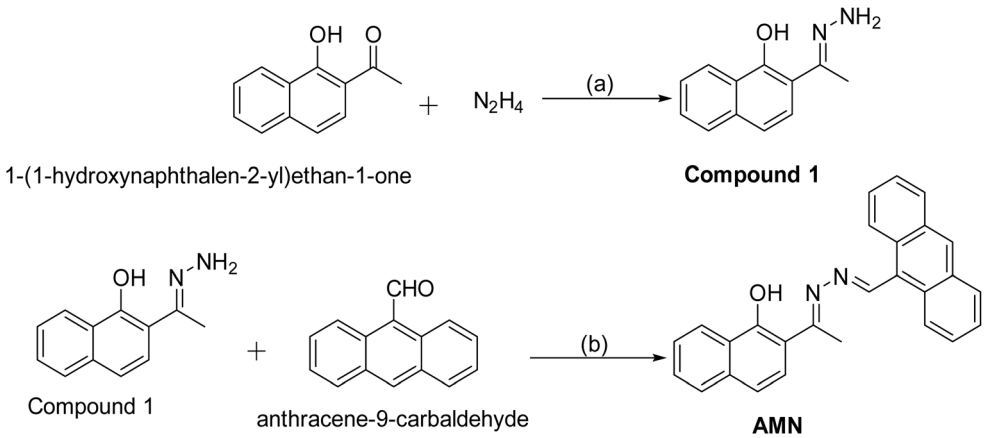

Scheme 1 Synthesis of **AMN**: (a) EtOH, rt, 24 h. (b) EtOH, rt, 48 h.

Hz), 8.41 (d, ^{1}H, J = 8 Hz), 8.21 (d, ^{1}H, J = 8.4 Hz), 7.91 (d, 2H, J = 8 Hz), 7.86 (d, ^{1}H, J = 8.8 Hz), 7.72 (d, ^{1}H, J = 6.8 Hz), 7.68 (d, 2H, J = 6 Hz), 7.64 (d, 3H, J = 7.2 Hz), 7.60 (d, ^{1}H, J = 7.6 Hz), 7.47 (d, ^{1}H, J = 8.8 Hz), 2.88 (s, 3H). Mass (m/z, %): M^+ calculated for chemical formula: $C_{27}H_{20}N_2O$ is 388.16; found: 389.95 $(M + H)^+$.

3. Results and discussion

3.1 Spectroscopic response of probe AMN toward NH_3 and PA

The spectrophotometric and spectrofluorometric titration of **AMN** with NH_3 and PA were conducted in CH_3CN/HEPES buffer (7 : 3, v/v, pH 7.4). The stability of the fluorescence of **AMN** is almost same in different ratios of CH_3CN/HEPES buffer mixtures and the spectrofluorimetric titration showed comparable emission changes (Fig. S14). Initially, the probe **AMN** showed a weak absorption peak at 365 nm, but with incremental addition of picric acid, the absorption band at 365 nm increased gradually in a dose dependent manner and naked eye color changes from colorless to pale yellow (Fig. 1). In case of spectrophotometric study of **AMN** in presence of NH_3, there is a slight decrease of absorbance at 365 nm (Fig. S15).

In the fluorescence spectroscopy, the sensing capabilities of **AMN** towards various analytes were examined in a CH_3CN/HEPES buffer mixture (7 : 3, v/v, pH 7.4) at an excitation wavelength of 364 nm. Primarily, **AMN** exhibited a strong emission band at 427 nm. However, upon the gradual incremental addition of PA, the emission intensity got reduced by 3-fold, accompanied by the appearance of a red shifted emission band at 463 nm ($\Delta\lambda$ = 36 nm) (Fig. 2a).

Conversely, when NH_3 was incrementally introduced in the solution of **AMN**, a fluorescence turn-on with 3-fold intensity increase was observed. The progressive addition of NH_3 led to a gradual increment in the emission band at 427 nm, with the appearance of a new red-shifted emission band emerged at 435 nm ($\Delta\lambda$ = 8 nm) (Fig. 2c). Binding isotherm of **AMN** with PA and NH_3 has been presented at 427 nm and 432 nm respectively (Fig. 2b and d).

The limit of detections of **AMN** towards PA and NH_3 have been calculated to be 8.77 μM and 5.29 μM, respectively, using the formula DL = $K \times Sb_1/S$, in which S is the calibration curve's slope and Sb_1 is the blank solution's standard deviation (Fig. S1 and S2).[42] Based on the first order rate equation and the variations of fluorescence intensity of **AMN** caused by the addition of PA and NH_3 at various time intervals, the rate constants were determined to be 143.24 s^{-1} and 330.41 s^{-1} respectively demonstrating the fast response of **AMN** towards PA and NH_3 (Fig. S5 and S6). The Stern–Volmer quenching constant (K_{SV}) was calculated to assess quenching efficiency and sensitivity. For PA the predicted the quenching constant (K_{SV}) values are 5.62 $\times 10^5$ M^{-1} (Fig. S7). This high quenching constant value indicates that PA have very good fluorescence quenching abilities towards **AMN**.

3.2 Interference study

To evaluate the selectivity of **AMN** towards PA, fluorescence experiments were conducted with **AMN** in the presence of various interfering nitroaromatic compounds in CH_3CN/HEPES buffer mixture (7 : 3 v/v, pH 7.4). Notably, upon the addition of PA to the receptor solution, the fluorescence intensity was significantly quenched, leading to a diminished emission signal at 427 nm. However, when other interfering nitroaromatic compounds such as dinitrobenzene (DNB), nitrobenzene (NB), 4-nitrotoluene (4-NT), 4-nitroaniline (4-NA), 4-nitrobenzoic acid (4-NBA), 1-chloro-2-nitrobenzene (1,2-CNB), and 2,4-dinitroanisole (2,4-DNAN) were introduced, no discernible fluorescence changes were observed (Fig. 3a).

This indicates that **AMN** exhibits high selectivity for PA. In the bar representation, the brown bar with lower intensity represents the fluorescence signal response of **AMN** with PA, while other brown bars with higher intensities indicate no significant interference in fluorescence of **AMN** with other interfering analytes (Fig. 3b).

Alternatively, the selectivity of **AMN** towards NH_3 has been justified by conducting a fluorescence experiment with various interfering anions like Cl^-, CH_3COO^-, Br^-, F^-, NO_2^-, $C_2O_4^-$, SO_4^{2-}, H_2O_2, NO_3^-, OCl^-, triethylamine (TEA), ethylenediamine (EDA), N_2H_4, piperidine (bpy) in CH_3CN : HEPES buffer (7 : 3, v/v, pH 7.4). Significantly, the presence of NH_3 in the **AMN**

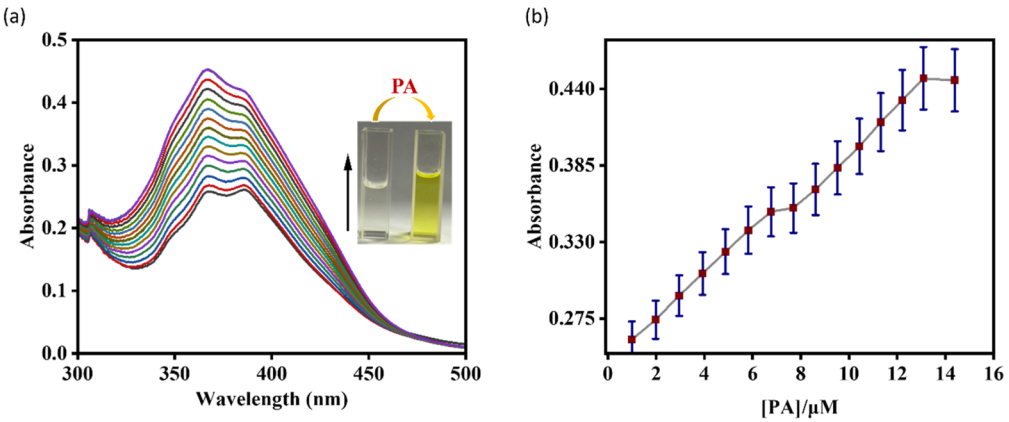

Fig. 1 (a) UV-vis titration spectra of **AMN** (c = 20 μM) with picric acid (c = 200 μM). (b) Absorbance changes of **AMN** as a function of picric acid concentration (error quantity, 5%; Y error bar for both [±] deviation).

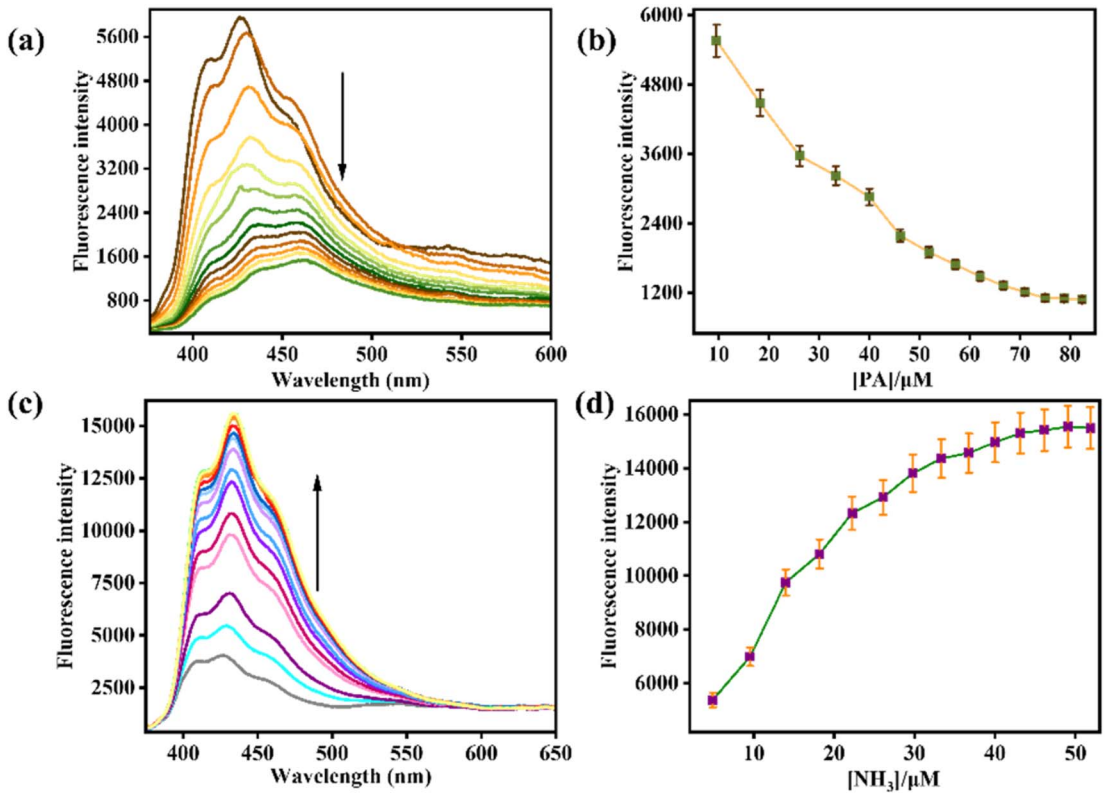

Fig. 2 (a) Fluorescence titration spectra of **AMN** ($c = 20$ μM) with PA ($c = 200$ μM). (b) The changes of emission intensity with variation of PA concentration along with error bars (error amount, 5%; *Y* error bar for both [±] deviation). (c) Fluorescence titration spectra of **AMN** ($c = 20$ μM) with NH_3 ($c = 200$ μM). (d) The changes of emission intensity with variation of NH_3 concentration along with error bars (error amount, 5%; *Y* error bar for both [±] deviation).

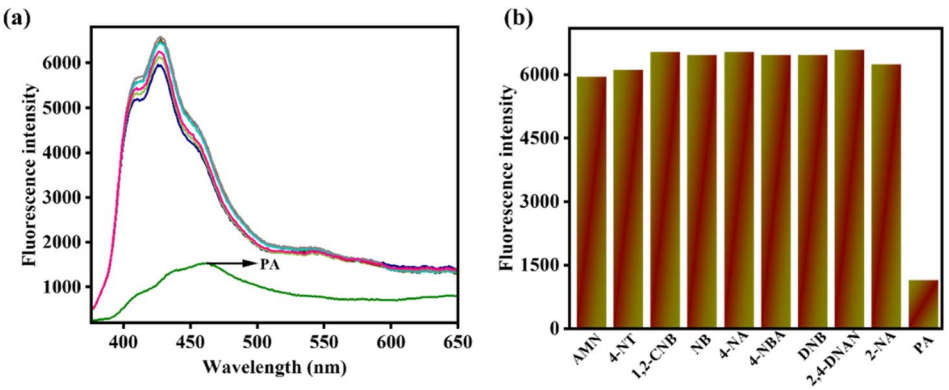

Fig. 3 (a) Comparison fluorescence spectra of **AMN** ($c = 20$ μM) upon addition of different guest analytes ($c = 200$ μM) (15 equiv.) at excitation at 364 nm. (b) Comparison fluorescence spectra of **AMN** upon addition of different guest analytes in bar diagram.

solution led to the appearance of a turn-on fluorescence response. However, upon the addition of all interfering analytes, the emission intensity at 427 nm remained unchanged. This finding demonstrates the remarkable selectivity of **AMN** for NH_3 (Fig. 4a). In the bar representation, the green bar with lower intensity indicates the fluorescence signal response of **AMN** with NH_3, while other blue bars with higher intensities indicate no notable interference in fluorescence of **AMN** with other interfering analytes (Fig. 4b).

3.3 Plausible binding mechanism of AMN with picric acid and ammonia

To elucidate the binding of **AMN** with picric acid and ammonia, UV-vis, fluorescence and ^{1}H NMR studies were performed in DMSO-d_6. In the absence of analytes, the ligand **AMN** exhibits strong orange fluorescence due to the conversion of the enol intermediate to the keto form through an ultrafast photo-induced tautomerization process *via* excited-state

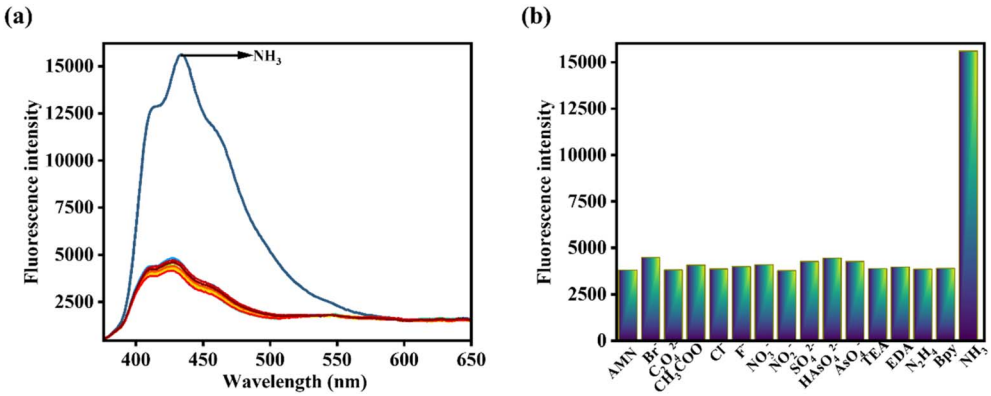

Fig. 4 (a) Comparison fluorescence spectra of AMN ($c = 20$ μM) upon addition of different guest analytes ($c = 200$ μM) (15 equiv.) at excitation at 364 nm. (b) Comparison fluorescence spectra of AMN upon addition of various different analytes in bar diagram.

intramolecular proton transfer (ESIPT). This process involves the transfer of a proton from the acidic hydroxyl group to the basic imine nitrogen, facilitated by the formation of a six-membered transition state (pathway A, Scheme 2). Upon exciting at 364 nm, **AMN** exhibits strong naked eye orange fluorescence in solid state with an intense emission signal at 629 nm (Fig. S16). In solution phase, **AMN** displays a strong absorbance signal at 365 nm and an emission signal at 427 nm, with a large Stokes shift of approximately 62 nm, which indicates the occurrence of the ESIPT phenomenon within the molecule.[43] However, the changes in absorption and fluorescence upon exposure to picric acid and ammonia are attributed to the suppression of the ESIPT process due to the strong interactions between the hydroxyl group of **AMN** with ammonia and picric acid.

Picric acid is a strong acid due to the high stability of its conjugate base, which is stabilized by extensive delocalization of the negative charge across the three nitro groups. Although picric acid can serve as both a hydrogen bond donor and acceptor, its conjugate base arises from proton loss and is strongly stabilized by the electron-withdrawing nitro substituents. The hydroxyl (–OH) group enables hydrogen bond donation, while the nitro oxygen atoms facilitate hydrogen bond acceptance, a property that is effectively exploited in the detection of picric acid.[44] Therefore, in the presence of picric acid, **AMN** exhibited enhanced absorbance and decreased fluorescence, attributed to the strong hydrogen bonding interactions between the nitro groups of picric acid and the hydroxyl group of **AMN** (pathway B, Scheme 2). This interaction was further supported by ^{1}H NMR experiments and theoretical studies. In the ^{1}H NMR experiments due to this strong interaction, the addition of PA to a solution of **AMN** resulted in a significant downfield shift of the phenolic hydroxyl proton signal and the decrease in electron density due to hydrogen bonding caused extensive broadening of the hydroxyl proton signal, shifting it from δ 15.25 ppm to δ 15.55 ppm. Additionally, other aromatic proton signals exhibited slight downfield shifts due to the formation of the **AMN-PA** charge transfer complex (Fig. S11).

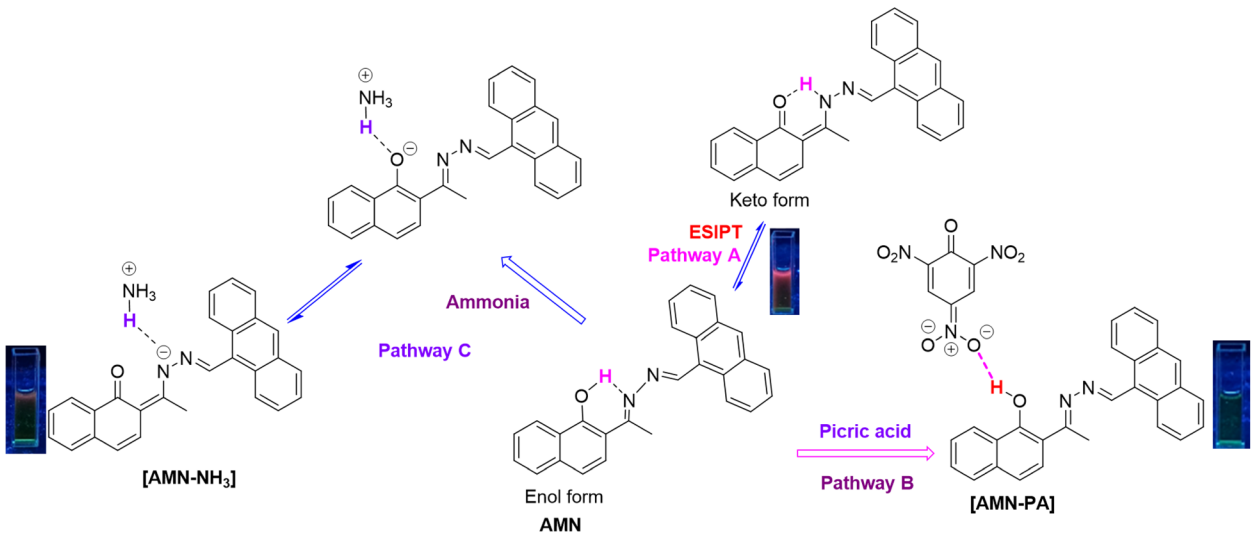

Scheme 2 Probable binding mechanism of AMN with PA and NH_3.

On the other hand, **AMN** displayed turn on fluorescence response due to the strong basicity of ammonia, which led to the deprotonation of the hydroxyl group, forming a 1-naphthoxide ion stabilized by resonance through the imine moiety (pathway C, Scheme 2). This deprotonation was validated by ^{1}H NMR studies, where, in the presence of NH_3, the hydroxyl proton signal at δ 15.25 ppm was almost completely diminished, while other aromatic proton signals shifted downfield, exhibiting higher δ values (Fig. S12).

3.4 Theoretical study

To explain the interactions mechanism between **AMN** with NH_3 and PA, we have performed structure optimization of **AMN** and **AMN-PA**, **AMN-NH$_3$** complexes using DFT calculations with B3LYP/6-31G (d,p) level of theory in the Gaussian 09 W software package (Experimental details in SI). The optimization of the ligand **AMN** and its complexes was carried out by generating a starting model based on the DFT-optimized structures of **AMN**, **AMN-PA**, and **AMN-NH$_3$** complexes (Fig. 5). Consistent with ^{1}H NMR observations, a strong hydrogen bonding interaction was identified between the hydroxyl group of **AMN** and the nitro group of PA. The **AMN** exhibited a notable energy gap of 7.3 eV between HOMO (−8.23 eV) and LUMO (−0.93 eV). However, upon interaction with PA and NH_3, the energy gaps were reduced to 2.94 eV (HOMO: −6.23 eV; LUMO: −3.29 eV) and 6.99 eV (HOMO: −8.16 eV; LUMO: −1.17 eV) respectively, indicating structural stabilization due to the strong interactions of **AMN** with PA and NH_3 (Fig. 6). For chemosensor **AMN**, the frontier molecular orbitals (FMOs) were primarily distributed over the more electron-rich anthracene moiety, resulting in only a modest intramolecular charge transfer (ICT) character. However, in the **AMN-PA** complex, a significant spatial separation of FMOs was observed. The HOMOs were mainly localized on the electron-deficient picric acid moiety, while the LUMOs were predominantly distributed along the **AMN** ligand. Similarly, for **AMN-NH$_3$** complex, the HOMOs were mainly localized on the naphthalene ring, while the LUMOs were predominantly distributed along the anthracene moiety of **AMN** ligand. This orbital distribution suggests strong interaction between **AMN** with PA and NH_3 within the complex, which affects the orbital distribution of LUMO and HOMO asymmetrically, thereby

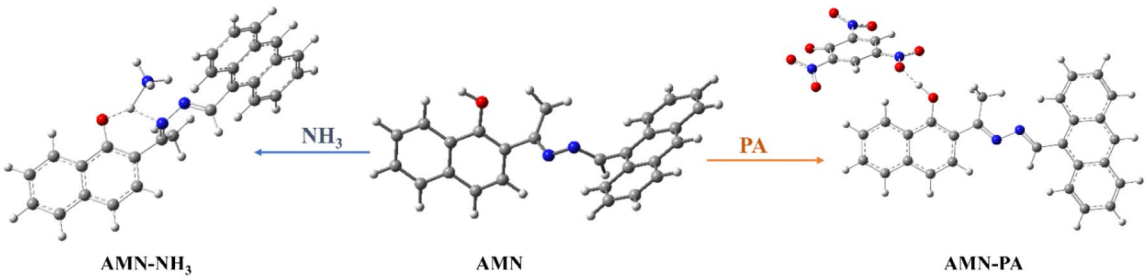

Fig. 5 Geometry optimized molecular structures of AMN, AMN-NH_3 complex and AMN-PA complex.

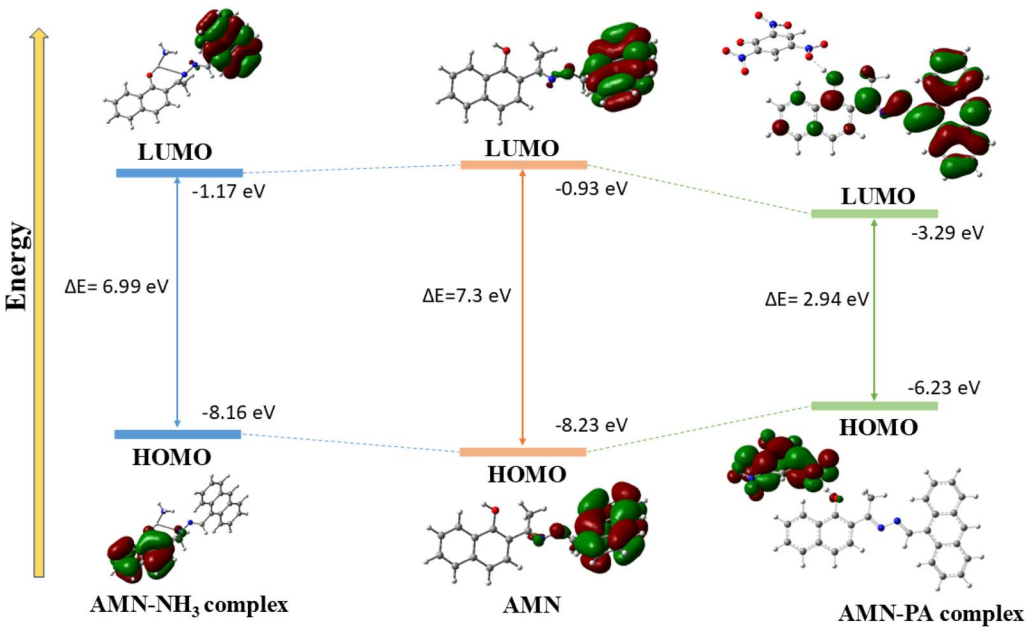

Fig. 6 Frontier molecular orbital with energy difference of AMN, AMN-PA complex and AMN-NH_3 complex.

influencing a notable optical response of **AMN** in presence of PA and NH_3.

3.5 Biological applications

3.5.1 DNA and protein binding studies. The binding properties of **AMN** with duplex ct DNA and Bovine Serum Albumin (BSA) were studied in Tris–HCl buffer (pH 7.2) using fluorescence and UV-vis spectral analysis. Initially, the ligand **AMN** exhibited a strong absorption signal at 395 nm. Upon increasing the concentration of BSA and ct DNA in the **AMN** solution, the absorption peak at 393 nm gradually decreased (Fig. 7a and 8a). Similarly, upon excitation at 418 nm, **AMN** showed a strong fluorescence with an emission signal at 625 nm. However, the incremental addition of ct DNA and BSA to the **AMN** solution led to a gradual decrement in fluorescence intensity at 625 nm with the appearance of a blue-shifted ratiometric fluorescence signal at 524 nm ($\Delta\lambda = 101$ nm), with an isoemission point at 568 nm. Although the ratiometric response of **AMN** with ct DNA is lower as compared to BSA (Fig. 7c and 8c). The limit of detection (LOD) of **AMN** for ct DNA and BSA was calculated to be 3.48 μM and 5.17 μM, respectively (Fig. S3 and S4). Based on a non-linear fluorometric binding isotherm, the binding constants of **AMN** with ct DNA and BSA were found to be 5×10^4 M^{-1} and 7.4×10^4 M^{-1} respectively (Fig. S17).

In order to further investigate the interaction mode between ct DNA and **AMN**, the competition assay mainly by replacement of intercalating dye like ethidium bromide (EB) from ct DNA was employed. Herein, the EB replacement assay has been performed by the fluorescence experiment in Tris–HCl buffer, pH = 7.2. Initially, high fluorescence intensity has been observed for EB bound ct DNA at 625 nm, which was significantly enhanced with the increase in concentrations of the compound **AMN**. This fluorescence enhancement is mainly due to the replacement of EB from EB bound ct DNA complex by **AMN**. This confirms the intercalation binding mode of **AMN** with ct DNA (Fig. S13). The significant changes in absorbance and ratiometric emission response of **AMN** in the presence of ct DNA and protein BSA are attributed to restricted conformational mobility, which minimizes non-radiative deactivation of the excited state. This phenomenon is consistent with previous observations for several styryl- and stilbene-based dyes.[45] Furthermore, the association of **AMN** is primarily driven by attractive dispersion forces, such as van der Waals interactions and π–π stacking, as well as the thermodynamically favorable release of counter-ions from DNA. These factors collectively restrict molecular flexibility and suppress the formation of ICT or CS excited states within the binding site.[46] Additionally, the polar binding cavities of DNA and proteins effectively stabilize the CS or ICT states, leading to ratiometric fluorescence.

3.5.2 *In silico* molecular docking studies. The binding interactions of **AMN** with ct DNA and BSA were further validated through molecular docking studies, a widely used method for speculating the binding affinity and interaction sites of

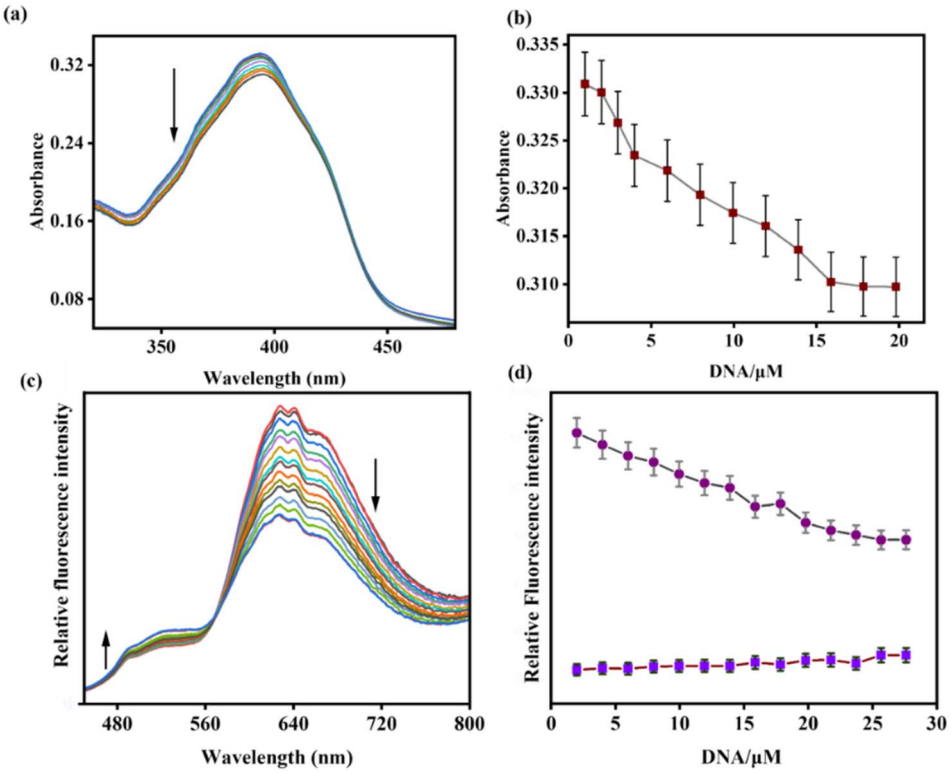

Fig. 7 (a) UV-vis and (c) fluorescence titration spectra of **AMN** ($c = 20$ μM) upon incremental addition of ct DNA ($c = 2$ mM in basepair) in Tris–HCl buffer, pH = 7.2. Plot of ct DNA concentration *vs.* intensity in (b) UV-vis and (d) fluorescence titration spectra (error quantity, 1% and 5% respectively; *Y* error bar for both [±] deviation).

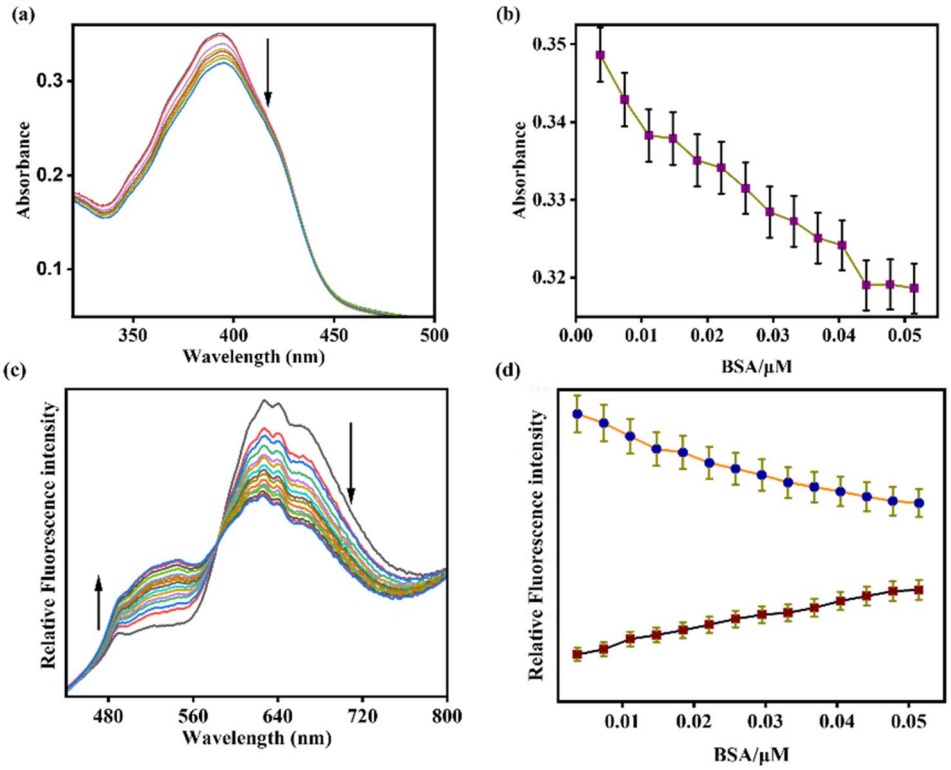

Fig. 8 (a) UV-vis and (c) fluorescence titration spectra of **AMN** ($c = 20$ μM) upon incremental addition of BSA ($c = 7.4$ μM) in Tris–HCl buffer, pH = 7.2. Plot of BSA concentration *vs.* intensity in (b) UV-vis and (d) fluorescence titration spectra (error quantity, 1% and 5% respectively; *Y* error bar for both [±] deviation).

biomolecules, including proteins and DNA. The docking simulations were performed using AutoDock Vina, which facilitated the analysis of the binding conformations of **AMN** with both BSA and ct DNA. Molecular docking studies revealed that **AMN** exhibited strong binding with the BSA protein through interactions with amino acid residues LYS211, ALA212, LEU326, ALA349, ASP323, GLY327, ARG208, LEU326, LYS350, and GLU353, with a binding affinity of -16.9 kcal mol^{-1} (Fig. 9a and b). Similarly, docking analysis of **AMN** with ct DNA indicated an intercalation binding mode, with a binding energy of

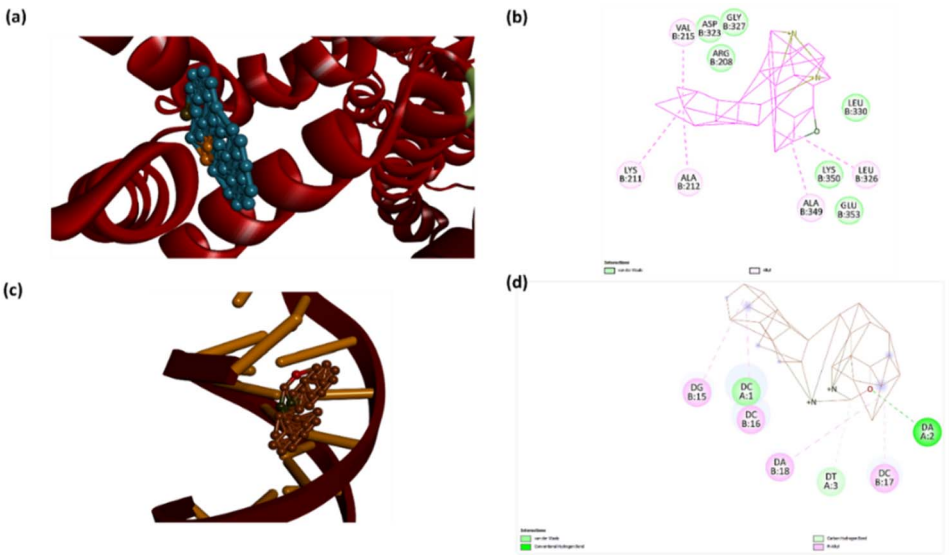

Fig. 9 Possible binding mechanisms of **AMN** with BSA and ct DNA. Ribbon (a) and (c) views of the BSA and ct DNA complexes, respectively; (b) and (d) represents two-dimensional interaction of BSA and DNA respectively.

−12.9 kcal mol^{-1} (Fig. 9c and d). The interaction between **AMN** and the DNA double helix was primarily established through deoxyribose guanine (15), deoxyribose thymine (3), deoxyribose cytosine (1, 16, 17), and deoxyribose adenine (2, 18) nucleosides (Fig. 9c and d). Overall, the docking studies suggest that **AMN** exhibits a strong binding affinity for both DNA and BSA, highlighting its potential as an effective biomolecular probe.

3.6 Practical application

3.6.1 Dipstick method (PA) and low-cost food spoilage indicator (NH_3). For the real-world application of the sensor **AMN**, dipstick method and low-cost food spoilage indicator experiments were performed for the detection of PA and NH_3 respectively. To evaluate the effectiveness of the **AMN** sensor for detecting PA, a dipstick method was employed using test strips prepared by immersing TLC plates in the receptor solution (c = 20 μM). Under UV light, the ligand exhibited a strong fluorescence, which significantly diminished upon the addition of PA, confirming the quenching property of **AMN** towards PA (Fig. 10a). Such dipsticks or test strips are advantageous as they allow for the immediate acquisition of qualitative data without requiring instrumental analysis.

Additionally, various volatile amines and ammonia vapors are released during food spoilage.[47] Freshly cut sardine fish were placed in glass bottles with **AMN**-coated filter sheets attached to the interior of the bottles to investigate the possible application of **AMN** for detecting biogenic volatile ammonia vapours (Fig. 10b). After three days of exposure to spoiled fish at 25 °C, the **AMN**-coated filter sheets were examined under 365 nm UV light. A significant enhancement in fluorescence intensity was observed, whereas in the absence of fish meat, the **AMN**-coated filter sheets retained the initial fluorescence (Fig. 10c). These results demonstrate that **AMN** exhibits high sensitivity and reactivity towards naturally generated ammonia vapors, enabling detection without the need for analytical instruments.

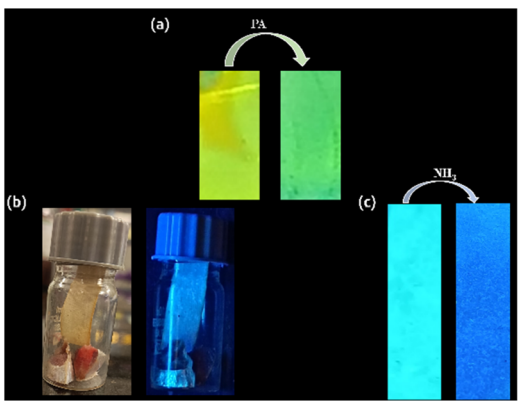

Fig. 10 (a) Photograph of TLC plates with **AMN** itself (left) (c = 20 μM) and presence of PA (right) (c = 200 μM). (b) The experimental setup of a paper strip placed above fresh fish (left) (naked eye view) and above spoiled fish (right) (under UV chamber), in glass vials covered tightly with a lid. (c) **AMN** coated test strips before exposure to NH_3 gas with fresh fish (left); after exposure to NH_3 gas from spoiled fish (right) under UV lamp.

4. Conclusion

In conclusion, the naphthalene–anthracene dyad (**AMN**) has been demonstrated as a highly effective dual fluorescence-based sensing approach for the detection of ammonia and picric acid. The selective fluorescence responses—turn-on bathochromic shift for NH_3 and turn-off quenching with a bathochromic shift for PA—enable easy visual and spectral detection of these analytes. The strong interactions between **AMN** with PA and NH_3 inhibiting the ESIPT process underpin the sensing mechanism, validated by extensive spectroscopic and computational analyses. Moreover, **AMN** displays a ratiometric fluorescence response when binding with BSA protein and ct DNA, along with notable alterations in its absorption spectra and the ability of **AMN** to interact with biomolecules further expands its scope for biochemical applications. For the practical applications of the sensor **AMN**, dipstick method and low-cost food spoilage indicator experiments were utilized for the detection of PA and NH_3 respectively without requiring any sophisticated instrumental analysis. Overall, **AMN** emerges as a promising and versatile fluorescence probe with significant potential for environmental and biomedical sensing.

Conflicts of interest

There are no conflicts of interest to declare.

Data availability

Supplementary information: The data supporting this article have been included as part of the SI. See DOI: **https://doi.org/10.1039/d5ra05068e**.

Acknowledgements

The authors gratefully acknowledge Christ University, Bangalore, for providing the necessary research facilities, and the Centre for Research, Christ University, for the seed money grant (Grant Approval Number: CU-ORS-SM-24/09). Avijit Kumar Das extends special thanks to the State University Research Excellence (SERB-SURE) program of the Science and Engineering Research Board (SERB) (File Number: SUR/2022/002461), under the Anusandhan National Research Foundation (ANRF) and the Department of Science and Technology (DST), Government of India, for financial support through the research grant. Malavika S. Kumar expresses her sincere appreciation to the University Grants Commission (UGC), Government of India, for awarding the Savitribai Jyotirao Phule Fellowship for Single Girl Child (SJSGC), F. No. 82-7/2022(SA-III).

References

1 J. Akhavan, *The Chemistry of Explosives*, Royal Society of Chemistry, Cambridge, England, 2nd edn, 2004, doi: DOI: **10.1039/9781847552020**.
2 (*a*) K. Spiegel, J. V. Headley, K. M. Peru, N. Haidar and N. P. Gurprasard, Residues of explosives in groundwater

leached from soils at a military site in eastern Germany, *Commun. Soil Sci. Plant Anal.*, 2005, **36**, 133–153, DOI: 10.1081/css-200043010; (*b*) S. Maredi, S. R. Nayak, M. I. Alam, D. Thakur and S. Vaidyanathan, *J. Mater. Chem. C*, 2025, **13**, 14333–14348.

3 (*a*) K. Ayoub, E. D. van Hullebusch, M. Cassir and A. Bermond, Application of advanced oxidation processes for TNT removal: A review, *J. Hazard. Mater.*, 2010, **178**, 10–28; (*b*) B. P. Debata, J. Dash, S. Patel and S. Vaidyanathan, *J. Mater. Chem. C*, 2025, **13**, 14385–14403.

4 B. Gogoi and N. Sen Sarma, Curcumin-cysteine and curcumin-tryptophan conjugate as fluorescence turn on sensors for picric Acid in aqueous media, *ACS Appl. Mater. Interfaces*, 2015, **7**, 11195–11202.

5 J. I. Steinfeld and J. Wormhoudt, Explosives detection: a challenge for physical chemistry, *Annu. Rev. Phys. Chem.*, 1998, **49**, 203–232, DOI: 10.1146/annurev.physchem.49.1.203.

6 M. E. Germain and M. J. Knapp, Optical explosives detection: from color changes to fluorescence turn-on, *Chem. Soc. Rev.*, 2009, **38**, 2543–2555, DOI: 10.1039/b809631g.

7 C. Beyer, U. Böhme, C. Pietzsch and G. Roewer, Preparation, characterization and properties of dipolar 1,2-N,N-dimethylaminomethylferrocenylsilanes, *J. Organomet. Chem.*, 2002, **654**, 187–201, DOI: 10.1016/s0022-328x(02)01427-4.

8 G. Jindal and N. Kaur, Fluorimetric quantification of picric acid in aqueous medium *via* smartphone and invisible ink applications using pyrene based sensor, Inorg, *Chem. Commun.*, 2022, **140**, 109481, DOI: 10.1016/j.inoche.2022.109481.

9 J. S. Caygill, F. Davis and S. P. J. Higson, Current trends in explosive detection techniques, *Talanta*, 2012, **88**, 14–29, DOI: 10.1016/j.talanta.2011.11.043.

10 (*a*) B. Roy, A. K. Bar, B. Gole and P. S. Mukherjee, Fluorescent tris-imidazolium sensors for picric acid explosive, *J. Org. Chem.*, 2013, **78**, 1306–1310, DOI: 10.1021/jo302585a; (*b*) S. R. Nayak, I. Siddiqui, Shahnawaz, J.-H. Jou and S. Vaidyanathan, *ACS Appl. Opt. Mater.*, 2023, **1**, 94–106.

11 (*a*) M.-A. Armour, *Hazardous Laboratory Chemicals Disposal Guide*, CRC Press, Boca Raton, FL, 3rd edn, 2003, doi: DOI: 10.1201/9781420032383; (*b*) S. R. Nayak, Shahnawaz, I. Siddiqui, J.-H. Jou, S. Patel and S. Vaidyanathan, *J. Phys. Chem. C.*, 2023, **127**, 499–515.

12 Y. Zhang, T.-G. Zhan, T.-Y. Zhou, Q.-Y. Qi, X.-N. Xu and X. Zhao, Fluorescence enhancement through the formation of a single-layer two-dimensional supramolecular organic framework and its application in highly selective recognition of picric acid, *Chem. Commun.*, 2016, **52**, 7588–7591, DOI: 10.1039/c6cc03631g.

13 J.-F. Xiong, J.-X. Li, G.-Z. Mo, J.-P. Huo, J.-Y. Liu, X.-Y. Chen and Z.-Y. Wang, Benzimidazole derivatives: selective fluorescent chemosensors for the picogram detection of picric acid, *J. Org. Chem.*, 2014, **79**, 11619–11630, DOI: 10.1021/jo502281b.

14 M. Dong, Y.-W. Wang, A.-J. Zhang and Y. Peng, Colorimetric and fluorescent chemosensors for the detection of 2,4,6-trinitrophenol and investigation of their co-crystal structures, *Chem. - Asian J.*, 2013, **8**, 1321–1330, DOI: 10.1002/asia.201300159.

15 K. P. Shrestha, L. Seidel, T. Zeuch and F. Mauss, Detailed kinetic mechanism for the oxidation of ammonia including the formation and reduction of nitrogen oxides, *Energy Fuels*, 2018, **32**, 10202–10217, DOI: 10.1021/acs.energyfuels.8b01056.

16 N. Tamaekong, C. Liewhiran, A. Wisitsoraat and S. Phanichphant, Flame-spray-made undoped zinc oxide films for gas sensing applications, *Sensors*, 2010, **10**, 7863–7873, DOI: 10.3390/s100807863.

17 S. Biring, A. S. Sadhu and M. Deb, An Effective Optical Dual Gas Sensor for Simultaneous Detection of Oxygen and Ammonia, *Sensors*, 2019, **19**, 5124, DOI: 10.3390/s19235124.

18 B. I. Cohen, The significance of ammonia/gamma-aminobutyric acid (GABA) ratio for normality and liver disorders, *Med. Hypotheses*, 2002, **59**, 757–758, DOI: 10.1016/s0306-9877(02)00325-0.

19 S. W. M. Olde Damink, N. E. P. Deutz, C. H. C. Dejong, P. B. Soeters and R. Jalan, Interorgan ammonia metabolism in liver failure, *Neurochem. Int.*, 2002, **41**, 177–188, DOI: 10.1016/S0197-0186(02)00040-2.

20 S. V. Krupa, Effects of atmospheric ammonia (NH_3) on terrestrial vegetation: a review, *Environ. Pollut.*, 2003, **124**, 179–221, DOI: 10.1016/s0269-7491(02)00434-7.

21 L. Peng, X. Yang, L. Yuan, L. Wang, E. Zhao, F. Tian and Y. Liu, Gaseous ammonia fluorescence probe based on cellulose acetate modified microstructured optical fiber, *Opt. Commun.*, 2011, **284**, 4810–4814, DOI: 10.1016/j.optcom.2011.06.015.

22 B. Zhao, J.-H. Bu, R. Zhang, M.-L. Shao, D.-Q. Wu and Z.-Y. Li, Syntheses, structures, and luminescent properties of two isostructural 3D CdII frameworks based on rigid-flexible hybrid ligands, Z. Anorg, *Allg. Chem.*, 2020, **646**, 426–430, DOI: 10.1002/zaac.202000100.

23 X. Liu, Y. Xu and D. Jiang, Conjugated microporous polymers as molecular sensing devices: microporous architecture enables rapid response and enhances sensitivity in fluorescence-on and fluorescence-off sensing, *J. Am. Chem. Soc.*, 2012, **134**, 8738–8741, DOI: 10.1021/ja303448r.

24 R. Claps, F. V. Englich, D. P. Leleux, D. Richter, F. K. Tittel and R. F. Curl, Ammonia Detection by use of Near-Infrared Diode-Laser-Based Overtone Spectroscopy, *Appl. Opt.*, 2001, **40**, 4387–4394.

25 A. Daridon, M. Sequeira, G. Pennarun-Thomas, H. Dirac, J. P. Krog, P. Gravesen, J. Lichtenberg, D. Diamond, E. Verpoorte and N. F. de Rooij, Chemical sensing using an integrated microfluidic system based on the Berthelot reaction, *Sens. Actuators, B*, 2001, **76**, 235–243, DOI: 10.1016/s0925-4005(01)00573-1.

26 J. L. Su, B. L. Schumacher, K. M. Lindley, V. Soloveychik, W. Burkhart, J. A. Triantafillou, K. Kuettner and T. Schmid, Detection of superficial zone protein in human and animal body fluids by cross-species monoclonal antibodies

specific to superficial zone protein, *Hybridoma*, 2001, **20**, 149–157, DOI: 10.1089/027245701750293475.

27 Z. Hu, B. J. Deibert and J. Li, Luminescent metal-organic frameworks for chemical sensing and explosive detection, *Chem. Soc. Rev.*, 2014, **43**, 5815–5840, DOI: 10.1039/c4cs00010b.

28 J. F. M. Oudenhoven, W. Knoben and R. van Schaijk, Electrochemical detection of ammonia using a thin ionic liquid film as the electrolyte, *Procedia Eng.*, 2015, **120**, 983–986, DOI: 10.1016/j.proeng.2015.08.636.

29 J. Wang, Z. Li, S. Zhang, S. Yan, B. Cao, Z. Wang and Y. Fu, Enhanced NH3 gas-sensing performance of silica modified CeO2 nanostructure based sensors, *Sens. Actuators, B*, 2018, **255**, 862–870, DOI: 10.1016/j.snb.2017.08.149.

30 C. Liu, H. Tai, P. Zhang, Z. Yuan, X. Du, G. Xie and Y. Jiang, A high-performance flexible gas sensor based on self-assembled PANI-CeO2 nanocomposite thin film for trace-level NH3 detection at room temperature, *Sens. Actuators, B*, 2018, **261**, 587–597, DOI: 10.1016/j.snb.2017.12.022.

31 P. R. Lakshmi, B. Mohan, P. Kang, P. Nanjan and S. Shanmugaraju, Recent advances in fluorescence chemosensors for ammonia sensing in the solution and vapor phases, *Chem. Commun.*, 2023, **59**, 1728–1743, DOI: 10.1039/d2cc06529k.

32 (*a*) A. Mondal, S. Mukhopadhyay, E. Ahmmed, S. Banerjee, E. Zangrando and P. Chattopadhyay, Understanding a thermoemissive ESIPT-based solid-state off–on switch as a dual-channel chemosensor in solid and solution phases: Detailed experimental and theoretical study, *J. Phys. Chem. C.*, 2020, **124**, 18181–18193, DOI: 10.1021/acs.jpcc.0c04603; (*b*) S. Vishnu, A. K. Das, G. Karan and S. M. Choudhury, Fluorescence Switching *via* Competitive ESIPT and Spirolactam Ring Opening in a Multifunctional Rhodamine B Probe for Selective Detection of Cu^{2+} and OCl^{-}: Theoretical Insights with Anticancer and Biosensor Activity, *Mater. Adv.*, 2025, **6**, 4499–4512; (*c*) S. Goswami, S. Maity, A. C. Maity, A. K. Das, B. Pakhira, S. Sarkar, K. Khanra and N. Bhattacharyya, ESIPT based Hg^{2+} and fluoride chemosensor for sensitive and selective 'turn on' red signal and cell imaging, *RSC Adv.*, 2015, **5**, 5735–5740.

33 (*a*) J. Guan, Q. Tu, L. Chen, M.-S. Yuan and J. Wang, A benzothiazole-rhodol based luminophor: ESIPT-induced AIE and an application for detecting Fe ion, *Spectrochim. Acta, Part A*, 2019, **220**, 117114, DOI: 10.1016/j.saa.2019.05.019; (*b*) S. Goswami, A. K. Das, A. Manna, A. K. Maity, H. K. Fun, C. K. Quah and P. Saha, A colorimetric and ratiometric fluorescent turn-on fluoride chemodosimeter and application in live cell imaging: high selectivity *via* specific Si–O cleavage in semi aqueous media and prompt recovery of ESIPT along with the Xray structures, *Tetrahedron Lett.*, 2014, **16**, 2633–2638; (*c*) S. Goswami, A. Manna, S. Paul, A. K. Das, P. K. Nandi, A. K. Maity and P. Saha, A turn on ESIPT probe for rapid and ratiometric fluorogenic detection homocysteine and cysteine in water with live cellimaging, *Tetrahedron Lett.*, 2014, **2**, 490–494; (*d*) S. Goswami, S. Maity, A. K. Das, A. C. Maity, T. K. Mandal and S. Samanta, Remarkable ESIPT induced NIR emission by a selective colorimetric dibenzimidazolo diimine sensor for acetate, *Tetrahedron Lett.*, 2013, **54**, 5232–5235.

34 (*a*) P.-T. Chou, Y.-C. Chen, W.-S. Yu, Y.-H. Chou, C.-Y. Wei and Y.-M. Cheng, Excited-state intramolecular proton transfer in 10-hydroxybenzo[h]quinoline, *J. Phys. Chem. A*, 2001, **105**, 1731–1740, DOI: 10.1021/jp002942w; (*b*) M. T. Ignasiak, C. Houée-Levin, G. Kciuk, B. Marciniak and T. Pedzinski, A reevaluation of the photolytic properties of 2-hydroxybenzophenone-based UV sunscreens: are chemical sunscreens inoffensive?, *Chemphyschem*, 2015, **16**, 628–633, DOI: 10.1002/cphc.201402703; (*c*) D. Ghosh, S. Batuta, S. Das, N. A. Begum and D. Mandal, Proton Transfer Dynamics of 4'-N,N-Dimethylamino-3-hydroxyflavone Observed in Hydrogen-Bonding Solvents and Aqueous Micelles, *J. Phys. Chem. B*, 2015, **119**, 5650–5661, DOI: 10.1021/acs.jpcb.5b00021; (*d*) S. J. Schmidtke, D. F. Underwood and D. A. Blank, Following the solvent directly during ultrafast excited state proton transfer, *J. Am. Chem. Soc.*, 2004, **126**, 8620–8621, DOI: 10.1021/ja048639g; (*e*) M. J. Paterson, M. A. Robb, L. Blancafort and A. D. DeBellis, Theoretical study of benzotriazole UV photostability: ultrafast deactivation through coupled proton and electron transfer triggered by a charge-transfer state, *J. Am. Chem. Soc.*, 2004, **126**, 2912–2922, DOI: 10.1021/ja0386593; (*f*) E. Hadjoudis and I. M. Mavridis, Photochromism and thermochromism of Schiff bases in the solid state: structural aspects, *Chem. Soc. Rev.*, 2004, **33**, 579–588, DOI: 10.1039/b303644h; (*g*) S. Goswami, A. Manna, S. Paul, A. K. Das, K. Aich and P. K. Nandi, Resonance-assisted hydrogen bonding induced nucleophilic addition to hamper ESIPT: ratiometric detection of cyanide in aqueous media, *Chem. Commun.*, 2013, **49**, 2912–2914.

35 S. Manna, E. Zangrando, H. Puschmann and S. C. Manna, Tetranuclear Schiff base copper(II) complexes: Syntheses, crystal structure, DNA/protein binding and catecholase-like activity, *Polyhedron*, 2019, **162**, 285–292, DOI: 10.1016/j.poly.2019.01.057.

36 A. K. Saini, P. Kumari, V. Sharma, P. Mathur and S. M. Mobin, Varying structural motifs in the salen based metal complexes of Co(ii), Ni(ii) and Cu(ii): synthesis, crystal structures, molecular dynamics and biological activities, *Dalton Trans.*, 2016, **45**, 19096–19108, DOI: 10.1039/c6dt03573f.

37 S. Gurusamy, R. Nandini Asha, M. Sankarganesh, T. Christopher Jeyakumar and A. Mathavan, Vanillin based colorimetric and fluorometric chemosensor for detection of Cu(II) ion: DFT calculation, DNA/BSA interaction and molecular docking studies, *Inorg. Chem. Commun.*, 2022, **143**, 109716, DOI: 10.1016/j.inoche.2022.109716.

38 C. Kalaivanan, M. Sankarganesh, M. Y. Suvaikin, G. B. Karthi, S. Gurusamy, R. Subramanian and R. N. Asha, Novel Cu(II) and Ni(II) complexes of nicotinamide based Mannich base: Synthesis, characterization, DFT calculation, DNA binding, molecular docking, antioxidant,

antimicrobial activities, *J. Mol. Liq.*, 2020, **320**, 114423, DOI: 10.1016/j.molliq.2020.114423.

39 S. Densil, C.-H. Chang, C.-L. Chen, A. Mathavan, A. Ramdass, V. Sathish, P. Thanasekaran, W.-S. Li and S. Rajagopal, Aggregation-induced emission enhancement of anthracene-derived Schiff base compounds and their application as a sensor for bovine serum albumin and optical cell imaging, *Luminescence*, 2018, **33**, 780–789, DOI: 10.1002/bio.3477.

40 F. Abyar and L. Tabrizi, Experimental and theoretical investigations of novel oxidovanadium(IV) juglone complex: DNA/HSA interaction and cytotoxic activity, *J. Biomol. Struct. Dyn.*, 2020, **38**, 474–487, DOI: 10.1080/07391102.2019.1580221.

41 M. Das, S. Mukherjee, B. Koley, I. Choudhuri, N. Bhattacharyya, P. Roy, B. C. Samanta, M. Barai and T. Maity, Developing novel zinc(ii) and copper(ii) Schiff base complexes: combined experimental and theoretical investigation on their DNA/protein binding efficacy and anticancer activity, *New J. Chem.*, 2020, **44**, 18347–18361, DOI: 10.1039/d0nj03844j.

42 M. Shortreed, R. Kopelman, M. Kuhn and B. Hoyland, Fluorescent fiber-optic calcium sensor for physiological measurements, *Anal. Chem.*, 1996, **68**, 1414–1418, DOI: 10.1021/ac950944k.

43 M. H. Lee, J. S. Kim and J. L. Sessler, Small molecule-based ratiometric fluorescence probes for cations, anions, and biomolecules, *Chem. Soc. Rev.*, 2025, **44**, 4185–4191, DOI: 10.1039/c4cs00280f.

44 S. Paul, P. Paul, S. Samanta, T. Majumdar and A. Mallick, *Org. Biomol. Chem.*, 2023, **21**, 3503–3524.

45 (*a*) R. W. Dirks and H. J. Tanke, Styryl molecules light-up RNAs, *Chem. Biol.*, 2006, **13**, 559–560, DOI: 10.1016/j.chembiol.2006.06.006; (*b*) C. V. Kumar, R. S. Turner and E. H. Asuncion, Groove binding of a styrylcyanine dye to the DNA double helix: the salt effect, *J. Photochem. Photobiol., A*, 1993, **74**, 231–238, DOI: 10.1016/1010-6030(93)80121-o; (*c*) A. K. Das, S. I. Druzhinin, H. Ihmels, M. Müller and H. Schönherr, Colorimetric and Fluorimetric DNA Detection with a Hydroxystyryl-Quinolizinium Photoacid and Its Application for Cell Imaging, *Chem. - Eur. J.*, 2019, **25**, 12703–12707, DOI: 10.1002/chem.201903017; (*d*) D. V. Berdnikova, O. A. Fedorova, E. V. Tulyakova, H. Li, S. Kölsch and H. Ihmels, Interaction of crown ether-annelated styryl dyes with double-stranded DNA, *Photochem. Photobiol.*, 2015, **91**, 723–731, DOI: 10.1111/php.12405.

46 A. Cuervo, P. D. Dans, J. L. Carrascosa, M. Orozco, G. Gomila and L. Fumagalli, Direct measurement of the dielectric polarization properties of DNA, *Proc. Natl. Acad. Sci. U. S. A.*, 2014, **111**, 3624–3630, DOI: 10.1073/pnas.1405702111.

47 T. Das, E. Joseph, M. S. Kumar, S. Vishnu, M. Dolai and A. K. Das, *Microchem. J.*, 2024, **199**, 110100, DOI: 10.1016/j.microc.2024.110100.